Acta Pharmaceutica Sinica B 2026;16(3):1717−1732

Chinese Pharmaceutical Association
Institute of Materia Medica, Chinese Academy of Medical Sciences

Acta Pharmaceutica Sinica B

www.elsevier.com/locate/apsb
www.sciencedirect.com

ORIGINAL ARTICLE

Exploiting eNOS activation to achieve tumor vascular normalization *via* endothelial transcytosis of lipid nanoparticles

Huisong Hao[a,†], Yunfei Yi[a,b,*,†], Yanan Fu[a], Shengjie Sun[a], Zhangwen Peng[a], Jia Tang[a], Yixuan Fang[a], Shihao Zhuang[a], Yaqi Ouyang[a], Tianqi Wang[a,*], Meiying Wu[a,*]

[a]*School of Pharmaceutical Sciences (Shenzhen), Shenzhen Campus of Sun Yat-sen University, Shenzhen 518107, China*
[b]*Tianjin Key Laboratory of Biomedical Materials, Key Laboratory of Biomaterials and Nanotechnology for Cancer Immunotherapy, Institute of Biomedical Engineering, Chinese Academy of Medical Sciences and Peking Union Medical College, Tianjin 300192, China*

Received 27 February 2025; received in revised form 25 May 2025; accepted 25 June 2025

KEY WORDS

Lipid nano delivery system;
Tumor vascular normalization;
Nitric oxide;
Endothelial NOS;
Endothelial cells;
Transcytosis;
Tumor microenvironment;
Immunotherapy

Abstract Abnormal tumor vasculature greatly accelerates tumor progression and diminishes antitumor treatments. Restoring perivascular NO gradients is available to maintain tumor vessel homeostasis and promote tumor vascular normalization. However, exogenously delivering NO strategies lacks the durability to maintain precise NO localization around tumor vessels. Herein, we design a lipid nano delivery system (MC@L) and exploit endothelial transcytosis to deliver metformin (Met) and CaO_2 into tumor vascular endothelial cells (ECs) and tumor cells for achieving tumor vascular normalization-boosted antitumor immunotherapies. The Ca^{2+} and Met released in ECs could restore perivascular localization of NO by activating endothelial NOS (eNOS). Additionally, MC@L internalized by tumor cells could cause CaO_2-induced immunogenic cell death (ICD), together with hypoxia relief and acid neutralization mediated by O_2 generation and H^+ consumption during CaO_2 degradation, thus further improving the immune effector cell functions under the accompaniment of Met-mediated inhibition of tryptophane uptake in tumor cells. Such a lipid nano delivery system greatly increases the susceptibility of 4T1 tumor-bearing mice to PD-L1 blockade efficacy.

*Corresponding authors.
E-mail addresses: b2023015006@pumc.edu.cn (Yunfei Yi), wangtq6@mail.sysu.edu.cn (Tianqi Wang), wumy53@mail.sysu.edu.cn (Meiying Wu).
†These authors made equal contributions to this work.

Peer review under the responsibility of Chinese Pharmaceutical Association and Institute of Materia Medica, Chinese Academy of Medical Sciences.

https://doi.org/10.1016/j.apsb.2025.11.040

1. Introduction

A key feature of the tumor microenvironment (TME) is the development of blood neovessels that nourish tumor growth; however, the unrestrained tumor angiogenesis driven by the imbalance between pro-angiogenic and anti-angiogenic signaling factors usually leads to tumor vasculature abnormality[1,2]. These abnormal vessels with irregular, chaotic, leaky, and compressed structures in turn function as the culprit of tumor expansion and metastasis. In addition, it has become a consensus that such a disordered tumor vasculature network contributes to the construction of the typical immunosuppressive TME featured with hypoxia, acidity, and interstitial fluid pressure (IFP), which is unfriendly for the infiltration and function of immune effector cells[3].

In the past years, anti-angiogenic therapy (AT) targeting neovessels has accomplished remarkable therapeutic values by blocking the pro-angiogenic factors like vascular endothelial growth factor (VEGF) and its corresponding receptors (VEGFR) using antibodies or small molecule antagonists[2]. However, the complete elimination of tumor vessels using high doses of AT agents usually traps AT in a vicious circle of angiogenesis and hypoxia[4]. As an updated practice, moderate AT modality could transiently normalize tumor vessels with improved functionality, which favors drug delivery and immunosuppressive TME reversion[4]. Among the tumor vascular normalization strategies that utilize antibodies or small molecule antagonists, the administration doses and time are the major considerations and obstacles. Alternatively, as a gaseous signaling molecule, nitric oxide (NO) is reported to play an essential role in angiogenesis and vessel maturation, thus possessing great potential in tumor vascular normalization[5]. Nowadays, numerous studies have explored the possibility of normalizing tumor vessels by restoring perivascular NO gradients through exogenous delivery of NO donors. Nevertheless, the time-dependent accumulation of NO donors might bring about NO aggregation at the far tumor regions rather than vascular endothelial cells (ECs), which is harmful to the maintenance of perivascular NO gradients. Therefore, there is an urgent need to identify new therapeutic modes for achieving precise NO localization around tumor vessels to enhance the tumor vascular normalization effect.

Generally, physiological NO is produced by the cellular NO synthase (NOS), which possesses three isoforms in different cells to perform specific functions, including neuronal NOS (nNOS, encoded by NOS1), inducible NOS (iNOS, encoded by NOS2), and endothelial NOS (eNOS, encoded by NOS3)[5,6]. In particular, the vascular ECs-derived eNOS could catalyze intracellular substrate L-arginine into NO[7], which would naturally localize around vessels to form perivascular NO gradients and benefit the perivascular cell recruitment, as well as vessel stabilization and maturation[5]. Instead of artificially delivering NO donors to restore the perivascular NO gradients, specifically improving the enzyme activity of tumor vascular ECs-localized eNOS might be a more promising strategy to induce sustained perivascular NO gradients for prolonged tumor vascular normalization. Functional eNOS is a dimer consisting of two identical subunits, each containing a reductase domain and an oxygenase domain, and these two domains are linked by a calmodulin (CaM)-binding sequence, which offers a binding site for Ca^{2+}/CaM complex to support the activation of eNOS[8-10]. Increasing the intracellular concentration of free Ca^{2+} could activate eNOS to enhance endothelial NO production by improving the Ca^{2+}/CaM complex binding with eNOS dimer to promote eNOS coupling for facilitating the alignment of the oxygenase and reductase domains[11]. In addition, other regulators such as activated adenosine monophosphate (AMP) -activated protein kinase (AMPK) could also benefit eNOS activation to promote NO production by increasing the phosphorylation of eNOS at Ser1177 residue. As a crucial cellular energy sensor functioning in maintaining energy homeostasis, endothelial AMPK could be activated by various stimuli, including energy-sensing molecules (*e.g.*, SIRT1), hormones (*e.g.*, adiponectin), and pharmacological activators (*e.g.*, metformin (Met))[12,13]. In general, modulators that cause adenosine monophosphate (AMP) or calcium accumulation are classified as indirect activators of AMPK. For example, Met could inhibit complex I of the mitochondrial respiratory chain to cause an increased AMP/ATP ratio, thus indirectly enhancing AMPK activity by phosphorylation at the Thr172 residue to upregulate eNOS phosphorylation and increase NO bioavailability[7,12,13]. Besides, Ca^{2+} also functions as an indirect activator of AMPK by activating its upstream kinase, Ca^{2+}/CaM-dependent protein kinase 2 (CaMKK2), which promotes the phosphorylation of the AMPKα catalytic subunit at the Thr172 residue[13]. Under such circumstances, it is foreseeable to achieve tumor vascular normalization *via* eNOS activation by promoting eNOS coupling and regulating the upstream kinase (phosphorylated AMPK) of eNOS phosphorylation to restore perivascular NO gradients.

Apart from participating in the construction of TME by developing tumor vasculature *via* generating NO and angiogenic factors, tumor vascular ECs also play a key role in transporting therapeutic agents to the tumor region. In the past, researchers put forward with enhanced permeability and retention (EPR) effect to explain the excellent tumor accumulation behavior of nanoparticles (NPs) to the tumor capillary fenestrations with sizes ranging from 200 to 2000 nm, which were peculiar in tumor regions owing to the tumor vasculature abnormality[14]. However, the latest studies revealed that in low-accumulating tumors featured with low vascular permeability (such as 4T1 tumor type), NPs entered tumor beds predominantly through active transport processes, including endothelial transcytosis and immune cell migration, rather than through inter-endothelial gaps[15-17]. Such effects were summarized as the active transport and retention (ATR) principle[16]. It is worth noting that endothelial transcytosis particularly plays an important role in transporting NPs across the tumor vasculature, and three endothelial transcytosis pathways have been identified, including intracellular vesicles (involving three steps: i. apical endocytosis, ii. intracellular transportation, and iii. basolateral exocytosis), vesiculo-vacuolar organelles (VVOs), and fenestrae[17]. The discovery of the ATR effect enlightened future research inspirations on therapies targeting tumor and tumor vascular ECs.

Given the enlightenment of the ATR principle that states the dominant role of endothelial transcytosis in the entry of NPs to low accumulating tumors and the superiority of lipid nanosystems

in the active transport of tumor vascular ECs by their unique physicochemical properties and biocompatibility, herein, we designed a lipid nano delivery system (MC@L) and exploited endothelial transcytosis to deliver CaO_2 and Met into tumor vascular ECs and tumor cells for vascular normalization, thus promoting the reversion of the hypoxic and acidic immunosuppressive TME (Scheme 1). Specifically, part of MC@L endocytosed by tumor vascular ECs *via* the intracellular vesicles pathway could first be sorted into early endosomes, then most of which underwent exocytosis (transcytosis), and the rest were transported to late endosomes/lysosomes for degradation to release Ca^{2+} and Met, thus activating eNOS of vascular ECs through Ca^{2+}-promoted eNOS coupling, and Ca^{2+} and Met-mediated AMPK—eNOS signaling pathway to restore perivascular NO gradients. While the majority of MC@L would undergo endothelial transcytosis *via* three pathways (intracellular vesicles, VVOs, and fenestrae) for further being internalized by tumor cells, which pososses lower pH values of lysosomes and deficient H_2O_2 detoxification ability, thus inducing Ca^{2+} overload and H_2O_2 accumulation-boosted oxidative stress for arousing immunogenic cell death (ICD). The consumption of H^+ during CaO_2 degradation in tumor cells could alleviate the acidity of TME. Moreover, Met-mediated downregulation of tryptophan (Trp) transporter SLC7A5 of tumor cells could further improve the immunosuppressive TME by hampering the transformation of Trp into kynurenine (Kyn), which is harmful to T cell proliferation and activity[18,19]. Overall, our lipid nano delivery system could successfully enable the extensive reversion of immunosuppressive TME by activating eNOS to establish tumor vascular normalization, causing severe oxidative stress and inhibiting Trp uptake of tumor cells to exhibit excellent antitumor efficacy when combined with PD-L1 blockade therapy.

2. Materials and methods

2.1. Materials

Calcium chloride dihydrate ($CaCl_2 \cdot 2H_2O$), 1,2-dioleoyl-*sn*-glycero-3-phosphocholine (DOPC), 1,2-di(*cis*-9-octadecenoyl)-*sn*-

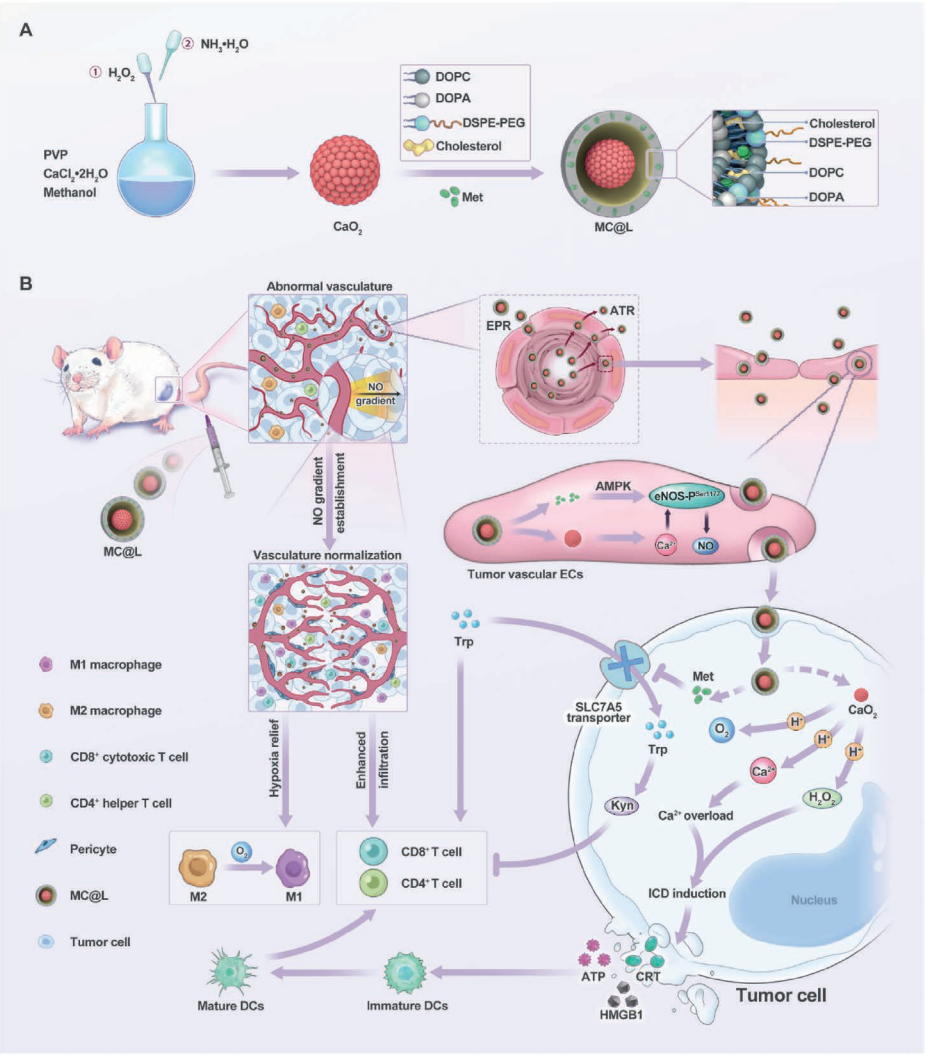

Scheme 1 Schematic illustration of lipid nano delivery system for eNOS activation-induced tumor vascular normalization *via* endothelial transcytosis. (A) Construction process of lipid nano delivery system (MC@L). (B) Proposed mechanism of MC@L-mediated tumor vascular normalization and antitumor therapy.

glycerol 3-phosphate sodium salt (DOPA), and cholesterol were purchased from Aladdin Scientific Crop (Shanghai, China). Ammonium hydroxide (25%−28%) was obtained from Sigma−Aldrich (Beijing, China). Methanol and hydrogen peroxide (H_2O_2, 30%) were provided by Guangzhou Chemical Reagent Co., Ltd. (Guangzhou, China). Metformin (Met) and poly(vinylpyrrolidone) (PVP, M.W. ≈ 58,000) were bought from Macklin Biochemical Co., Ltd. (Shanghai, China). 1,2-distearoyl-*sn*-glycero-3-phosphoethanolamine-*N*-[methoxy(polyethylene glycol)-2000] (DSPE-PEG2000) was obtained from Xi'an Ruixi Biological Technology Co., Ltd. (Xi'an, China). InVivoMAb anti-mouse PD-L1 was bought from Bio X Cell (Cat: BE0101, Clone: 10F.9G2TM). All chemical agents were used directly without further purification.

2.2. Synthesis of CaO_2 NPs

CaO_2 was synthesized according to the previous literature with a slight modification[20]. Typically, 200 mg $CaCl_2 \cdot 2H_2O$ and 60 mg PVP were dissolved in 60 mL of methanol. After mixing well, 400 μL of H_2O_2 (30%) was dripped into the suspension, and the reaction system was continuously stirred for 30 min. Subsequently, 1 mL of $NH_3 \cdot H_2O$ was poured into the mixture under vigorous stirring. After constant stirring for 20 min, CaO_2 was collected by centrifugation at 15,000 rpm for 15 min and washed three times with methanol.

2.3. Preparation of MC@L

MC@L was prepared by the thin film-hydration method. CaO_2 (5.6 mg) and Met (4.5 mg) were added to the chloroform solution of DOPC (3.93 mg), DOPA (3.62 mg), cholesterol (0.97 mg), and DSPE-PEG2000 (1.4 mg). After thoroughly mixing with the help of ultrasound, the solvent was completely evaporated under a rotary evaporator, and a thin lipid film was formed. Finally, the film was hydrated with 2 mL aqueous solution, and MC@L was obtained. M@L and C@L were prepared *via* the same protocol, apart from the absence of corresponding agents. The content of CaO_2 and Met was determined by Calcium Colorimetric Assay Kit (S1063S, Beyotime) and UV−Vis spectrophotometer (U7S, Yoke Instrument), respectively. The drug loading (DL) and encapsulation efficiency (EE) of CaO_2 and metformin were calculated according to Eqs. (1) and (2):

$$\mathrm{DL}\,(\%) = W/W_a \times 100 \quad (1)$$

$$\mathrm{EE}\,(\%) = W/W_b \times 100 \quad (2)$$

where W represents the quantity of CaO_2 and metformin loaded in nanoparticles, W_a represents the weight of nanoparticles, and W_b represents the total amount of CaO_2 and metformin added.

2.4. Characterization

The morphologies of different NPs were observed by transmission electron microscopy (TEM) (HT7800, Hitachi). The particle sizes and zeta potentials were determined by dynamic light scattering (DLS) using a Zetasizer Pro (Nano ZS, Malvern). The crystalline structure of different samples was determined with an X-ray diffractometer (XRD, SmartLab SE, Rigaku).

2.5. In vitro acidity neutralization

The acidity neutralization capacity of MC@L was evaluated by adding different amounts of MC@L (50, 100, 200, 400, and 800 μg/mL) into PBS with different pH values (5.5 or 6.5). After shaking (120 rpm) at 37 °C for 12 h, the pH values of the solutions were determined by a pH meter (Orion Star A211, Thermo Scientific).

2.6. In vitro pH-responsive Ca^{2+} release

The *in vitro* release of Ca^{2+} from MC@L was determined by the bag filter method. Briefly, MC@L was packaged into a dialysis bag and immersed in PBS solution with varied pH values (7.4, 6.5, or 5.5). After shaking at 37 °C for different times, 0.5 mL of the releasing solution was taken out to examine the concentration of Ca^{2+}, and 0.5 mL of fresh PBS buffer solution was replenished. The amount of released Ca^{2+} was tested by Calcium Colorimetric Assay Kit (S1063S, Beyotime).

2.7. In vitro H_2O_2 production

CaO_2 and MC@L were dispersed in PBS solution with different pH values (7.4, 6.5, or 5.5) and shaken at 37 °C for 1, 3, or 5 h. Then the solution was centrifuged at 14,000 rpm for 15 min, and the supernatant was tested by CheKine™ Micro Hydrogen Peroxide Assay Kit (KTB1041, Abbkine).

2.8. In vitro O_2 generation

To detect the generation of O_2, different amounts of MC@L (200, 400, 800, and 1600 μg/mL) were added to PBS solution (pH 5.5). After stirring for 1 h, the O_2 concentration was monitored with a portable dissolved oxygen meter (JPSJ-605F). As a control, the O_2 concentration in PBS solution was monitored under the same conditions.

2.9. Intracellular NO level

The intracellular NO level was investigated using the DAR-1 probe (ABS42016331, absin). Briefly, HUVECs were seeded in the confocal dishes with a density of 1.2×10^5 cells per well and cultured for 24 h at 37 °C under 5% CO_2 atmosphere, followed by different treatments. Afterward, the cells were washed three times with PBS and stained with 1 mL of DAR-1 probe (5 μmol/L) solution at 37 °C under 5% CO_2 atmosphere for 30 min. The cells were washed with PBS, and the intracellular fluorescence was observed using CLSM.

2.10. Tube formation assay

The tube formation assay was conducted to assess the inhibitory efficacy of MC@L on HUVEC vascularization. Briefly, HUVECs were seeded into Matrigel-coated 24-well plates (10^5 per well) with DMEM containing different formulations. 50 × Endothelial Cell Growth Supplement (ECGS) was added into the cell suspension in each group (the final concentration of ECGS was determined to be 0.5 ×). The HUVECs without drug treatment were set as the control group. After incubation at 37 °C under 5% CO_2 atmosphere for 4 h, the tubule formation was imaged by an inverted microscope, and the tubule length was calculated using ImageJ software.

2.11. Wound healing assay

HUVEC were inoculated into 6-well plates (3×10^5 cells per well) and cultured for 24 h at 37 °C under 5% CO_2 atmosphere. The cell-attached bottoms were uniformly and straightly scratched with a 200 μL pipette tip. Next, the cells were washed with PBS and incubated with DMEM containing different formulations. The scratched areas were visualized by an inverted microscope at different time points.

2.12. Cell cytotoxicity

HUVEC or 4T1 cells were seeded into 96-well plates (8×10^3 cells per well) and cultured for 12 h at 37 °C under 5% CO_2 atmosphere. Afterward, the cells were incubated with M@L, C@L, or MC@L with different concentrations (equivalent CaO_2 concentration was 18, 36, 72, 108, 144, and 180 μg/mL, equivalent Met concentration was 32, 65, 129, 194, 258, and 323 μg/mL). The untreated HUVEC or 4T1 cells were set as the control group. After incubation for 48 h, the cell viabilities of different groups were assessed using the standard CCK-8 method.

2.13. Transcytosis assay

For flow cytometry examination of Cy5 left in HUVEC and the extracellular content of Cy5 excreted by HUVEC, experiments at different times, HUVEC were seeded into 6-well plates (3×10^5 cells per well) and cultured for 24 h at 37 °C under 5% CO_2 atmosphere. The cells were first incubated with DMEM containing Cy5-MC@L (the concentration of Cy5 was 5 μg/mL) for 6 h. Next, the cells were washed with PBS and incubated with serum-free DMEM for different times (0, 0.5, 1, 2, 4, and 6 h). Afterward, the serum-free DMEM was collected for detecting the content of Cy5 excreted by HUVEC. The cells were collected by trypsin and examined using flow cytometry. For TEM analysis of intracellular NPs internalized by HUVEC and extracellular NPs excreted by HUVEC, HUVEC were seeded into 6-well plates (3×10^5 cells per well) and cultured for 24 h at 37 °C under 5% CO_2 atmosphere. The cells were first incubated with DMEM containing Cy5-MC@L (the concentration of Cy5 was 5 μg/mL) for 6 h. Next, the cells were washed with PBS and incubated with serum-free DMEM for 1 h. Afterward, the serum-free DMEM was collected and ultrafiltered; the condensed solution was used for TEM analysis of extracellular NPs excreted by HUVEC. Meanwhile, the cells were washed with PBS and also collected for TEM analysis of intracellular NPs internalized by HUVEC.

2.14. Intracellular Ca^{2+} release and H_2O_2 generation

To investigate the accumulation of intracellular Ca^{2+} and H_2O_2 levels in 4T1 cells, 4T1 cells were seeded in the confocal dishes with a density of 10^5 cells per well and cultured for 24 h at 37 °C under 5% CO_2 atmosphere, followed by different treatments. Afterward, the cells were washed three times with PBS. The intracellular Ca^{2+} and H_2O_2 levels were detected by CLSM after being stained by Fluo-4 AM (HY-101896, MCE) and ROSGreen H_2O_2 Probe (MX5202, MKBio), respectively.

2.15. Intracellular hypoxia relief

The intracellular levels of O_2 in 4T1 cells with different treatments were quantified to examine the relief of intracellular hypoxia. 4T1 cells were seeded in the confocal dishes with a density of 10^5 cells per well and cultured for 24 h at 37 °C under hypoxic condition, followed with different treatments for 4 h. Afterward, the cells were fixed with 4% paraformaldehyde and stained with luminescent oxygen sensor (MX4826, MKBio) before being stained with DAPI. Then the fluorescence of intracellular O_2 was visualized by CLSM.

2.16. Extracellular pH neutralization

For extracellular pH neutralization, 4T1 cells were seeded into 12-well plates (6×10^4 cells per well) and cultured for 24 h at 37 °C under 5% CO_2 atmosphere. Afterward, the cells were incubated with fresh culture medium or medium containing MC@L (equivalent CaO_2 concentration was 72 μg/mL) for different times (0, 12, 24, 36, 48, and 60 h). The blank culture medium placed in the carbon dioxide incubator was set as the negative control group. The old medium of treated cells and blank culture medium was then collected for further pH value detection using a pH meter.

2.17. Extracellular Trp levels

4T1 cells were seeded into 6-well plates (3×10^5 cells per well) and cultured for 24 h at 37 °C under 5% CO_2 atmosphere. The cells were incubated with DMEM containing different formulations. After incubation at 37 °C under 5% CO_2 atmosphere for 24 h, the cell culture medium was collected for measuring the content of Trp by ELISA (MM-0756M1, Meimian).

2.18. In vitro examination of ICD biomarkers

The examinations of surface-exposed CRT and nucleus-located HMGB1 were performed using CLSM. Briefly, 4T1 cells were seeded in confocal dishes (2×10^5 cells per dish) and cultured for 24 h at 37 °C under 5% CO_2 atmosphere. The cells were incubated with M@L, C@L, or MC@L (equivalent CaO_2 concentration was 72 μg/mL) for 24 h. The untreated 4T1 cells were set as the control group. Afterward, the cells were stained with anti-CRT or anti-HMGB1 antibody for observation by CLSM. For ATP detection, 4T1 cells were seeded into 6-well plates (2×10^5 cells per well) and cultured for 24 h at 37 °C under 5% CO_2 atmosphere. Subsequently, the cells were incubated with M@L, C@L, or MC@L (equivalent CaO_2 concentration was 72 μg/mL) for 24 h. The untreated 4T1 cells were set as the control group. After incubation, the cells were collected for further analysis using the Chemiluminescence ATP Determination Kit (E-BC-F002, Elabscience).

2.19. In vitro induction and cell viability of bone-marrow-derived DC (BMDC) maturation

To investigate the influences of different treatments on BMDC maturation *in vitro*, bone marrow cells were first isolated from the femurs of healthy female BALB/c mice aged 6−8 weeks. The collected bone marrow cells were seeded into 24-well plates (2×10^5 cells per well) and cultured with complete RPMI 1640 medium containing granulocyte-macrophage colony-stimulating factor (GM-CSF, 20 ng/mL) and interleukin-4 (IL-4, 20 ng/mL) for differentiation into immature BMDCs at 37 °C under 5% CO_2 atmosphere. On Day 5, the immature BMDCs were co-incubated with 4T1 cells in a transwell chamber, where 4T1 cells were treated with different formulations. After co-incubation for 48 h,

BMDCs were collected and stained with APC anti-mouse CD11c (Biolegend, 117310), PE anti-mouse CD80 (Biolegend, 104707), and FITC anti-mouse CD86 (Biolegend, 105006), followed by analyzing the DC maturation rates using flow cytometry. To investigate the cell viability of BMDCs, BMDCs were seeded in 96-well plates (8×10^3 cells per well). Fresh cell culture medium with MC@L (equivalent CaO_2 concentration was 72 μg/mL) under different pH values (pH 7.4, 6.5, and 5.5) was prepared with lactic acid. Then the BMDCs were incubated with the prepared cell culture medium for 24 h. Afterward, 10 μL CCK-8 was added to the culture medium per well and incubated for 1 h. The absorbance at 450 nm was detected to assay the cell viability of BMDCs.

2.20. *In vitro macrophage repolarization*

Bone marrow cells were first isolated from healthy BALB/c mice. The collected bone marrow cells were seeded into 12-well plates (1.5×10^6 cells per well) and cultured with complete DMEM medium containing M-CSF (20 ng/mL) for differentiation into immature BMDM cells at 37 °C under 5% CO_2 atmosphere. On Day 6, the old medium was replaced with fresh DMEM containing IL-4 (20 ng/mL) to induce the polarization of BMDM towards the M2 phenotype after incubation for 24 h. The obtained cells were subsequently incubated with DMEM containing different formulations for 24 h under hypoxic conditions. The cells were collected and stained with APC750 anti-CD11b (Biolegend, 101262), PE anti-F4/80 (Biolegend, 123110), APC anti-CD206 (Biolegend, 141708), and PE anti-CD86 (Biolegend, 105006) for M1 and M2 macrophage detection.

2.21. *Animal model*

6−8 weeks old female BALB/c mice were purchased from Zhuhai Bes Test Bio-Tech Co., Ltd. All animal experimental procedures were executed according to the protocols approved by the Institutional Animal Care and Use Committee of Sun Yat-sen University (Approval No. SYSU-YXYSZ20220329). To establish the 4T1 tumor-bearing mice model, 1×10^6 4T1 cells were suspended in 100 μL PBS and subcutaneously injected into the left mammary gland of each mouse.

2.22. *Biosafety evaluation*

For the *in vivo* biosafety assessment, healthy BALB/c mice aged 6−8 weeks were intravenously injected with MC@L, and the body weight changes were recorded. After 14 days of injection, the whole blood samples and the serum were collected for blood routine test and blood biochemistry analysis.

2.23. *In vivo tumor vessel normalization*

To test intratumoral NO and angiogenesis, 4T1 tumor-bearing BALB/c mice were intravenously injected with M@L, C@L, and MC@L (10 mg/kg CaO_2, 18 mg/kg Met). After 12 h, the mice were killed, and the tumor tissues were collected. Then, the expression of eNOS in tumor tissues was measured by ELISA (MM-0455M2, Meimian). The content of NO in tumor vessels was detected by the co-staining of anti-CD31 (28083-1-AP, Proteintech) and DAR-1 (ABS42016331, absin). In addition, the relief of tumor hypoxia (bsm-62534R, Bioss) and the expression of VEGF (BM3995, Boster) were also analyzed by immunofluorescence staining. To analyze the perfusion of tumor vessels, 4T1 tumor-bearing BALB/c mice were intravenously injected with M@L, C@L, and MC@L (10 mg/kg CaO_2, 18 mg/kg Met) for 12 h. Then the mice were intravenously injected with FITC-lectin (1 mg/mL, 100 μL). After 20 min, the mice were sacrificed, and the tumors were collected for immunofluorescence staining of anti-CD31 and DAPI.

2.24. *In vivo biodistribution and Ca^{2+} accumulation*

For the *in vivo* biodistribution assay, free Cy5 and Cy5-MC@L were intravenously injected into the 4T1 tumor-bearing mice at an equivalent Cy5 dose of 3 mg/kg. At certain time intervals (2, 12, and 24 h) after injection, the mice were imaged by the In-Vivo Imaging System (Lumina II, PerkinElmer). The mice were euthanized after 24 h of injection, and the tumors and major organs (heart, liver, spleen, lung, and kidney) were dissected for *ex vivo* imaging. For the *in vivo* Ca^{2+} accumulation assay, 4T1 tumor-bearing mice were intravenously injected with C@L and MC@L (equivalent CaO_2 dose was 10 mg/kg). The mice were euthanized after 24 h of injection, and the content of Ca^{2+} in major organs and tumor tissues was determined by Calcium Colorimetric Assay Kit (S1063S, Beyotime). The content of Ca^{2+} in major organs and tumor tissues of 4T1 tumor-bearing mice with no treatment was set as the control.

2.25. *Distribution of MC@L in tumor tissue*

To track the distribution of MC@L in tumor tissue, Cy5-labeled MC@L (Cy5-MC@L) was intravenously injected into the 4T1 tumor-bearing mice (3 mg/kg Cy5). At certain time intervals (1, 2, 6, 12, and 24 h) after injection, the mice were killed and the tumor tissues were collected. Then the tumor tissues were sectioned and co-stained with anti-CD31 (28083-1-AP, Proteintech) to assess the distribution of MC@L in tumors.

2.26. *In vivo antitumor efficacy*

4T1 tumor-bearing mice were randomly divided into 6 groups and intravenously administered with PBS, αPD-L1, M@L, C@L, MC@L, and MC@L+αPD-L1 (10 mg/kg CaO_2, 18 mg/kg Met, 5 mg/kg αPD-L1) every 4 days to investigate the tumor inhibition effects. During the treatments, the tumor size and body weight were recorded every 2 days. The tumor size was calculated according to Eq. (3):

$$\text{Tumor volume} = (\text{Tumor length}) \times (\text{Tumor width})^2 / 2 \ (\text{mm}^3) \quad (3)$$

At the end of *in vivo* treatments, the major organs (heart, liver, spleen, lung, and kidney), tumors, and tumor-draining lymph nodes of the mice were collected for further analysis.

2.27. *In vivo immune response analysis*

The single-cell suspension of tumors and lymph nodes was first prepared for immune cell analysis. For DC maturation analysis, the single-cell suspension of lymph nodes was stained with APC anti-mouse CD11c (Biolegend, 117310), PE anti-mouse CD80 (Biolegend, 104707), and FITC anti-mouse CD86 (Biolegend, 105006). For T-lymphocyte analysis, the single-cell suspension of tumors was stained with APC anti-mouse CD3 (Biolegend,

100236), FITC anti-mouse CD4 (Biolegend, 100406), and PE anti-mouse CD8a (Biolegend, 100707). For macrophage analysis, the single-cell suspension of tumors was stained with APC750 anti-CD11b (Biolegend, 101262), PE anti-F4/80 (Biolegend, 123110), APC anti-CD206 (Biolegend, 141708), and PE anti-CD86 (Biolegend, 105006). For regulatory T cell analysis, the single-cell suspension of tumors was stained with APC anti-mouse CD3 (Biolegend, 100236), FITC anti-mouse CD4 (Biolegend, 100406), and PE anti-mouse Foxp3 (Biolegend, 126404). Moreover, the contents of IFN-γ, TNF-α, and IL-10 in tumors were measured by ELISA kits from Solarbio following the manufacturer's instructions.

2.28. *Statistical analysis*

The results were presented as mean $\pm$ standard deviation (SD). A two-tailed unpaired Student's *t*-test and one-way ANOVA were used to analyze the statistical differences. Significant values were implied as below: $^{*}P < 0.05$, $^{**}P < 0.01$, $^{***}P < 0.001$. ns, no significance.

3. Results and discussion

3.1. *Preparation of MC@L NPs*

CaO_2 NPs were first synthesized *via* a wet chemistry method[20]. According to the transmission electron microscope (TEM) image (Fig. 1A), the fabricated CaO_2 NPs displayed uniform morphology with nanoscale sizes. Afterward, Met and CaO_2 NPs were separately or together encapsulated by lipid to construct the lipid nano delivery system (designated as M@L, C@L, and MC@L). The TEM image of MC@L exhibited a distinct shell compared with that of CaO_2 NPs (Fig. 1A and B), and the elemental mapping image of MC@L confirmed the existence of N element in the shell and Ca, O elements in the core (Supporting Information Fig. S1). Compared with MC@L, M@L exhibited a typical liposome structure with a uniform spherical shape, while the morphology of C@L was similar to MC@L, presenting a distinct core-shell structure (Supporting Information Fig. S2A and S2B). Similarly, the hydrodynamic diameters of C@L (114.70 $\pm$ 0.46 nm) and MC@L (112.37 $\pm$ 0.71 nm) were also consistent, and slightly larger than

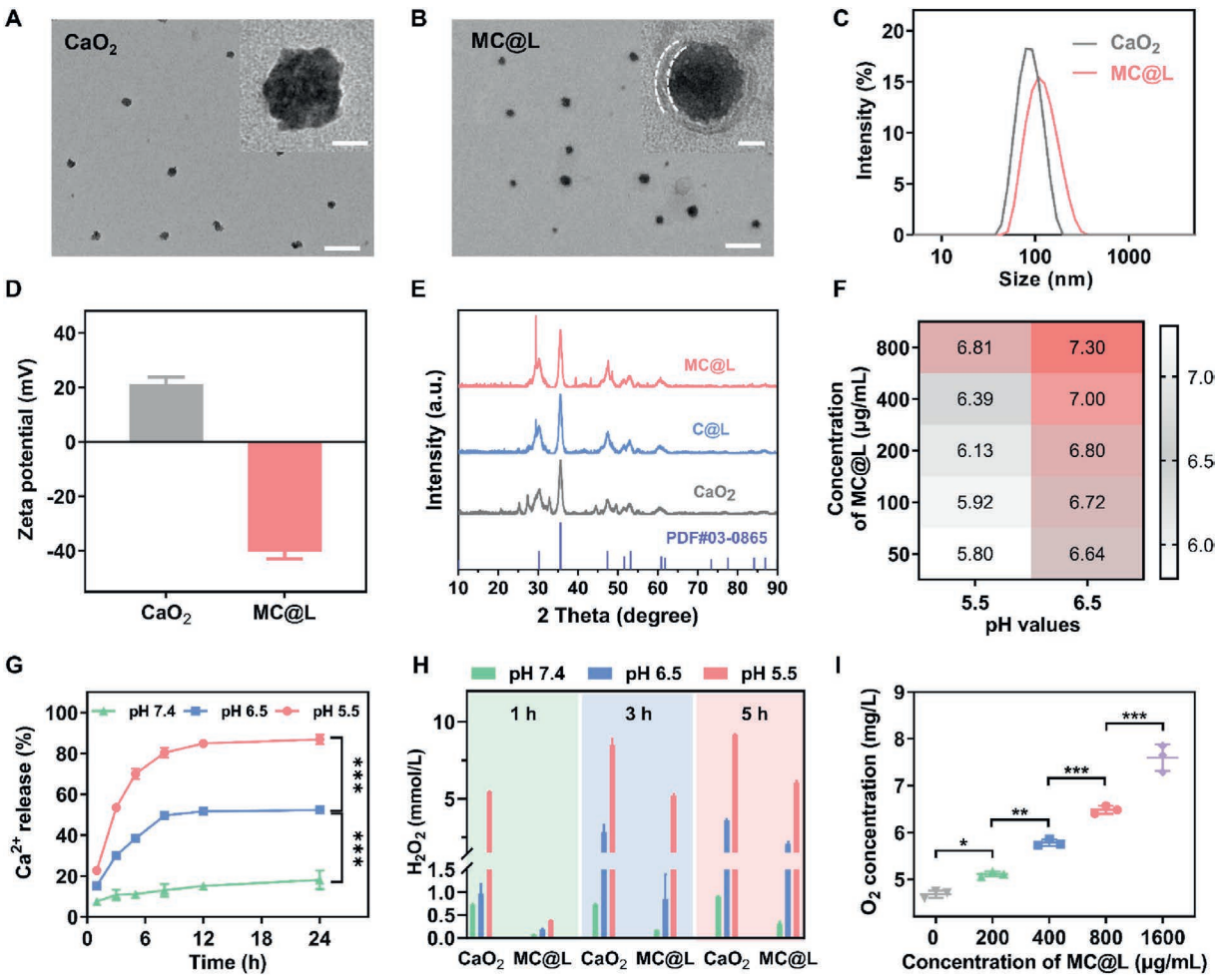

Figure 1 Preparation and characterization of MC@L. (A, B) TEM images of CaO_2 (A) and MC@L (B). Scale bar = 200 or 20 nm (enlarged images). (C) The hydrodynamic particle sizes of CaO_2 and MC@L were determined by DLS. (D) Zeta potentials of CaO_2 and MC@L. (E) XRD pattern results of CaO_2, C@L, and MC@L. (F) *In vitro* acidity neutralization of MC@L. (G) *In vitro* Ca^{2+} release from MC@L under different pH conditions. (H) *In vitro* H_2O_2 production of CaO_2 and MC@L under different pH conditions at different time points. (I) *In vitro* O_2 generation of MC@L at different concentrations. Data are presented as mean $\pm$ SD ($n = 3$). $^{*}P < 0.05$, $^{**}P < 0.01$, $^{***}P < 0.001$.

that of CaO_2 NPs (83.08 ± 0.73 nm) and M@L (83.10 ± 1.45 nm) (Fig. 1C and Fig. S2C). Compared to the positive zeta potential of CaO_2 NPs (21.26 ± 2.47 mV), the zeta potential of M@L, C@L, and MC@L decreased to −23.08 ± 0.64 mV, −31.68 ± 0.89, and −40.48 ± 2.47 mV, respectively (Fig. 1D and Fig. S2D). In addition, the powder X-ray diffraction (XRD) pattern results verified that the encapsulation of CaO_2 into MC@L did not affect the crystal structure of CaO_2, indicating the successful fabrication of MC@L (Fig. 1E). According to the standard curves shown in Supporting Information Fig. S3, the drug loading of CaO_2 and Met in MC@L was calculated to be 7.76 ± 0.21% and 13.62 ± 0.36%. The encapsulation efficiency of CaO_2 and Met was 24.96 ± 3.65% and 48.69 ± 1.74%, respectively. Moreover, the hydrodynamic diameter of MC@L showed almost no change during the 72-h storage in DMEM containing 10% FBS, suggesting the excellent physiological stability of MC@L (Supporting Information Fig. S4).

Owing to the alkaline property, CaO_2 NPs could degrade into Ca^{2+} and H_2O_2 when encountering H^+, thus holding the potential to perform Ca^{2+} overload-mediated oxidative stress injury in tumor cells, which possess lower pH values of lysosomes than those of normal cells. Meanwhile, as one of the reactive oxygen species (ROS), H_2O_2 could also increase the burden of oxidative stress. To investigate the acid degradability of MC@L, an *in vitro* acidity neutralization experiment was carried out by incubating MC@L with PBS (pH 5.5 or 6.5). As shown in Fig. 1F, the pH values of the incubation solutions went up with the increasing concentration of MC@L, proving the excellent acidity neutralization capability of MC@L and indicating its potential for improving the acidic TME. Next, pH-responsive Ca^{2+} release and H_2O_2 production behavior of MC@L were further examined. As verified in Fig. 1G and H, the degradation of MC@L was positively correlated with the acidity of the incubation buffer, which met the prerequisite for achieving Ca^{2+} overload and oxidative stress injury in tumor cells. As a competitive process, CaO_2 NPs could decompose into Ca^{2+} and O_2 in the acidic environment as well[21], thus contributing to the relief of the hypoxic TME. To investigate the O_2 generation capability of MC@L, the concentration of O_2 was subsequently measured by a portable dissolved oxygen meter after MC@L was dispersed in the PBS buffer (pH 5.5) for 1 h, and obvious dose-dependent O_2 generation was observed (Fig. 1I).

3.2. *In vitro anti-angiogenesis*

Tumor angiogenesis functions as the prerequisite process for promoting tumor invasion and metastasis. In order to evaluate the potential of our fabricated lipid nano delivery system on reversing the tumor vasculature abnormality, the antiangiogenic effects were first studied on human umbilical vein endothelial cells (HUVEC) *in vitro*. Considering that eNOS plays a crucial role in mediating tumor vascular normalization, and the phosphorylation of eNOS at Ser1177 (designated as eNOS-$P^{Ser1177}$) close to the carboxyterminal is critical for the activation of eNOS that further catalyzes substrate L-arginine into NO (Fig. 2A)[7], the eNOS-$P^{Ser1177}$ expression levels were initially examined. As illustrated in Fig. 2B, both Met and Ca^{2+} could enhance AMPK activity by phosphorylation at the Thr172 residue (Supporting Information Fig. S5A), which further activated its downstream eNOS protein through increasing phosphorylation of eNOS at Ser1177. And the detailed mechanism for AMPK activation has been reported that Met could inhibit complex I of the mitochondrial respiratory chain to cause an increased AMP/ATP ratio[12,13], and Ca^{2+} could activate CaMKK2 (Fig. S5B), an upstream kinase of AMPK[13], thus both of which functioning as indirect activators of AMPK. As Fig. 2C indicates, both M@L and C@L enhanced the eNOS-$P^{Ser1177}$ expressions compared to control group, and C@L showed slightly better eNOS activation effect than M@L, which was not only ascribed to Ca^{2+}-mediated AMPK activation, but also took advantage of the direct activation effect of Ca^{2+} on eNOS by improving the binding of Ca^{2+}/CaM complex with eNOS dimer, thus promoting eNOS coupling for facilitating the alignment of the oxygenase and reductase domains[11]. It's worth noting that MC@L exhibited the highest expression level of eNOS-$P^{Ser1177}$ among all the groups, verifying the synergistic effect of CaO_2 and Met. Fig. 2D further revealed that the elevated eNOS-$P^{Ser1177}$ expression was consistent with the NO production in HUVEC, thus demonstrating the feasibility of inducing perivascular NO gradients by activating vascular EC-localized eNOS.

NO functions as a crucial gaseous signaling molecule in anti-angiogenesis and vessel maturation. To evaluate the anti-angiogenesis of the lipid nano delivery system, angiogenesis-related genes in HUVEC with different treatments were analyzed using qPCR. It turned out that two pro-angiogenic genes (VEGF and platelet-derived growth factor subunit B (PDGFB)) were down-regulated, and one maturation-related gene (angiopoietin 1, Ang1) was upregulated in Met or CaO_2-contained groups (Fig. 2E, Supporting Information Figs. S6 and S7), suggesting that the treatment of inducing eNOS-catalyzed NO by Met or Ca^{2+} may contribute to reprogramming the gene expressions of ECs from pro-angiogenic to vascular-stabilizing phenotype in solid tumors. Furthermore, tube formation and migration assays that indicate the angiogenesis capabilities of HUVEC were carried out to evaluate the vascular normalization potential *in vitro*. As shown in Fig. 2F and G, and Supporting Information Figs. S8 and S9, single Met or CaO_2-contained group exhibited inhibitory effects on tube formation and cell migration to different degrees when compared to the control group, and MC@L group displayed the most remarkable anti-angiogenesis efficiency, which indicated the synergistic effect of Met and CaO_2 on inhibiting angiogenesis activity of ECs.

Considering that the degradation products of CaO_2 (Ca^{2+} and H_2O_2) may cause severe cellular injury to HUVEC and result in the collapse of tumor vasculature, which is disadvantageous for achieving tumor vascular normalization, the cellular viability of HUVEC was subsequently analyzed. As shown in Fig. 2H, the cell viability of HUVEC was maintained at a high level (81.09 ± 5.63%) in MC@L group at the therapeutic dose (72 μg/mL CaO_2), verifying the biosafety of our fabricated lipid nano delivery system in normal cells and the potential to induce tumor vascular normalization *in vivo*.

3.3. *In vitro transcytosis*

Based on the ATR principle which states that the dominant mode of NPs entry to tumors is more active than passive in low accumulating tumors featured with low vascular permeability[16], such as 4T1 and U87 tumor types[15], we exploited the transcytosis effect to transport our fabricated lipid nano delivery system to 4T1 tumor cells through tumor vascular ECs for subsequent antitumor therapy. To investigate the transcytosis function of ECs, we incubated HUVEC with Cy5-labelled MC@L (Cy5-MC@L) for 6 h to ensure enough engulfment of NPs, then replaced the culture medium with fresh serum-free medium for different times to detect the extracellular content of Cy5 excreted by HUVEC and the intracellular content of Cy5 left in HUVEC. According to Fig. 2I and J, and Supporting Information Fig. S10, the intracellular and

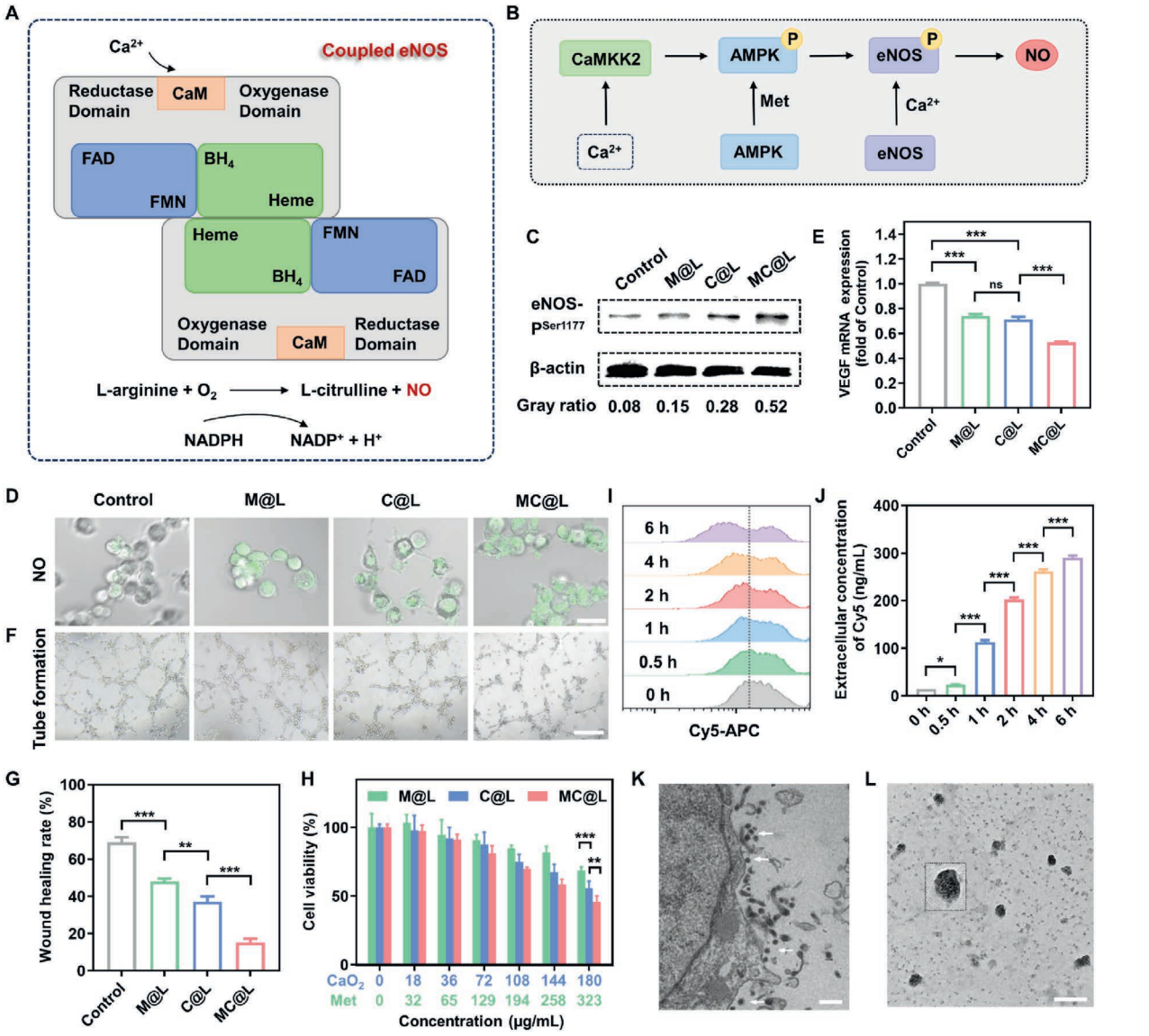

Figure 2 *In vitro* anti-angiogenesis and transcytosis in HUVEC. (A) Schematic diagram of coupled eNOS (O_2: oxygen; NADPH: nicotinamide adenine dinucleotide phosphate hydroxide; $NADP^+$: nicotinamide adenine dinucleotide phosphate; FAD: flavin adenine dinucleotide; FMN: flavin mononucleotide; CaM: calmodulin). (B) Schematic diagram of the signaling pathway of eNOS-mediated NO catalysis. (C) Western blotting analysis of eNOS-$P^{Ser1177}$ expression levels in HUVEC with different treatments. (D) CLSM examination of intracellular NO generation in HUVEC with different treatments. Scale bar = 30 μm. (E) mRNA expressions of VEGF in HUVEC with different treatments were analyzed by qPCR. (F) The tube formation of HUVEC after 4 h incubation with different treatments. Scale bar = 500 μm. (G) The quantification of wound healing in HUVEC with different treatments (n = 3). (H) HUVEC viability after 48 h incubation with different treatments (n = 5). (I) Flow cytometry examination of Cy5 left in HUVEC after being incubated for 6 h with Cy5-MC@L, and then replaced and incubated with fresh serum-free medium for different times. (J) The final extracellular content of Cy5 excreted by HUVEC after being incubated for 6 h with Cy5-MC@L first, and then replaced and incubated with fresh serum-free medium for different times. (n = 3). (K) TEM images of HUVEC treated with MC@L-contained medium for 6 h and then with replaced fresh serum-free medium for 1 h (white arrows indicated NPs in the cytoplasm region, which were close to the dark grey nucleus). Scale bar = 500 nm. (L) TEM images of extracellular serum-free supernatant cultured with HUVEC after incubation with MC@L-contained medium for 6 h and then with replaced fresh serum-free medium for 1 h. Scale bar = 250 nm. Data are presented as mean ± SD. *$P < 0.05$, **$P < 0.01$, ***$P < 0.001$. ns, no significance.

extracellular content of Cy5 decreased and increased, respectively, as the incubation time went by, verifying the successful transcytosis of our fabricated lipid nano delivery system, which may be further engulfed in tumor cells and perform subsequent therapeutic effects.

In order to better visualize the transcytosis effect, HUVECs that were treated with MC@L for 6 h, followed by replacement with fresh serum-free medium to incubate for 1 more hour, together with the corresponding replaced serum-free medium, were collected for TEM analysis. As indicated in Fig. 2K, L, and Supporting Information Fig. S11, the existence of nanosized NPs within the cytoplasm region of HUVEC and in the replaced serum-free medium further verified the successful transcytosis of NPs by HUVEC, which supported our assumption that exploiting

endothelial transcytosis to enhance subsequent calcium overloading-mediated therapeutic modality in tumor cells.

3.4. In vitro immune activation

Given the importance of Ca^{2+} in numerous cellular processes, including proliferation, metabolism, and death, the burst of Ca^{2+} overload at cellular levels could result in calcium signaling disorders, which further function as manipulators to cause cell death[22]. As a consequence, Ca^{2+} overload strategies have been widely researched to study their antitumor efficacy[23,24]. In order to verify the capability of CaO_2 encapsulated within our lipid nano delivery system to degrade into Ca^{2+} in acidic lysosomes of tumor cells, the intracellular Ca^{2+} accumulation in 4T1 cells was examined. As shown in Fig. 3A and Supporting Information Fig. S12A, the CaO_2-contained groups (C@L and MC@L) could effectively induce Ca^{2+} overload compared to the control group and M@L groups. And owing to the lower pH value of tumor cell lysosomes (pH $\approx$ 4.2) than normal cell lysosomes ($\approx$4.8)[25-27], MC@L induced a larger amount of Ca^{2+} release in 4T1 cells than normal cells (Fig. S12A). In addition, the intracellular H_2O_2 content in 4T1 cells was demonstrated to be positively correlated with the Ca^{2+} content (Fig. 3B), which was beneficial for increasing Ca^{2+} overload-mediated oxidative stress and inducing tumor cell death. To be worth noting, 4T1 cells exhibited higher basal levels of H_2O_2 (control group) compared to HUVECs, and also less excellent H_2O_2 detoxification capability when treated with MC@L (Fig. S12B). Such a phenomenon was ascribed to that, compared to non-transformed cells, most cancer cells exhibit lower basal levels of antioxidant enzymes, and display reduced activity of both catalase (CAT) and glutathione peroxidase (GPx), and also higher H_2O_2 concentration[28,29]. As the other product of CaO_2 degradation, O_2 was subsequently detected. According to Fig. 3C, both C@L and MC@L groups exhibited remarkable improvement of hypoxia alleviation in 4T1 cells, indicating the potential of our fabricated lipid nano delivery system in alleviating the anaerobic state of the TME by generating O_2 *in situ*. In particular, it was worth noting that the degradation of MC@L charged with an abundance of H^+ (Fig. 3D), thus benefiting the reversion of immunosuppressive TME by alleviating the acidic TME. The cytotoxicity of our fabricated lipid nano delivery system was much higher in 4T1 cells than in HUVEC, owing to the acidic preference of CaO_2 degradation (Fig. 3E and 2H).

In addition to functioning as the eNOS activator in ECs, Met also engages in regulating antitumor immunity by inhibiting Trp uptake through downregulating MYC, which further results in the reduction of the Trp transporter SLC7A5 (Fig. 3F)[19]. As shown in Fig. 3G, the Met-contained groups exhibited decreased SLC7A5 mRNA expressions to different degrees, thus exhibiting distinct inhibitory effects on Trp uptake by 4T1 cells (Fig. 3H). Evidence has proven that Trp participates in constructing the immunosuppressive TME by being catalyzed to Kyn by the overexpressed indoleamine 2,3-dioxygenase (IDO) enzyme, which is harmful to the proliferation and activity of T cells[30]. It was interesting that the C@L group also exhibited slightly decreased SLC7A5 mRNA expression compared to the control group, and we supposed that such a phenomenon might be driven by the injured viability of tumor cells whose signal transduction was severely disturbed by Ca^{2+} overload.

Emerging evidence identified that Ca^{2+} overload and oxidative stress mediated by CaO_2 in tumor cells could induce ICD by accelerating the release of danger-associated molecular patterns (DAMPs), which function as "danger signals" for the host immune system to promote the maturation of DCs and arouse specific T lymphocyte-mediated antitumor immunity[31-33]. On that account, three typical DAMPs, including surface-exposed calreticulin (CRT), nucleus-released high mobility group box 1 (HMGB1), and released adenosine triphosphate (ATP), were selected as indicators to assess ICD effect mediated by our lipid nano delivery system. As shown in Fig. 3I and J, control and M@L groups had negligible or limited effects on eliciting CRT exposure on the plasma membrane, as well as HMGB1 and ATP release into the extracellular environment, while C@L and MC@L groups exhibited a substantial increase of CRT exposure and significant release of HMGB1 and ATP, proving the successful CaO_2-mediated ICD induction in tumor cells.

Subsequently, the potential of DC maturation was further investigated by incubating the pre-treated 4T1 cells with bone marrow-derived dendritic cells (BMDCs). Compared to control (15.9%) and M@L (16.6%) groups (Fig. 3K and Supporting Information Fig. S13), both C@L and MC@L groups displayed higher percentages of DC maturation (24.9% and 36.7% respectively), which proved that CaO_2 could effectively improve the tumor cell immunogenicity. The synergistic effect of Met and CaO_2 contributed to the highest DC maturation, which could be perceptibly observed according to the optical images (Fig. 3L). Considering that the degradation of CaO_2 consumed abundant H^+, which was harmful to the normal functions of immune cells (Fig. 1F and 3D), the positive impact of acidity neutralization mediated by lipid nano delivery system was further investigated by detecting the DCs' viability. As indicated in Supporting Information Fig. S14, the DCs treated with MC@L exhibited higher cellular viability under the acidic incubating condition (pH 6.5 and 5.5) than DCs without any treatments, proving that the improvement of acidic environment was beneficial for DCs' survival.

Additionally, it has also been reported that O_2 is available to reprogram pro-tumoral M2 phenotype toward anti-tumoral M1 phenotype, thus contributing to the improvement of immunosuppressive TME *in vivo*[1,34]. Given that O_2 is the product of CaO_2 degradation, we subsequently examined the repolarization of M2 macrophages to M1 phenotype under hypoxia conditions. An obvious decrease of M2 macrophages and an increase of M1 macrophages in CaO_2-contained groups were observed according to Fig. 3M, N, and Supporting Information Fig. S15, demonstrating that the alleviation of hypoxia was indeed conducive to reprogramming M2 macrophages. It was noteworthy that M@L also displayed a remarkable repolarization effect compared to the control group, which might be ascribed to the Met-mediated AMPK−NF-κB signaling pathway, according to the reported research.

3.5. In vivo vascular normalization and biodistribution

Before carrying out *in vivo* experiments, the biosafety of MC@L was first evaluated by monitoring the body weight changes, blood biochemistry parameters, and complete blood count. The results displayed that the injection of MC@L did not induce significant changes in the body weight and the main indicators of heart, liver, and kidney function (Supporting Information Fig. S16A and S16B). In addition, the complete blood count of mice revealed no abnormal alterations in immune cell counts, indicating MC@L did not cause abnormal immune activation (Fig. S16C−S16J). These results demonstrated the excellent biosafety of MC@L and supported the subsequent *in vivo* applications. Inspired by the excellent anti-angiogenesis and immunoregulation results

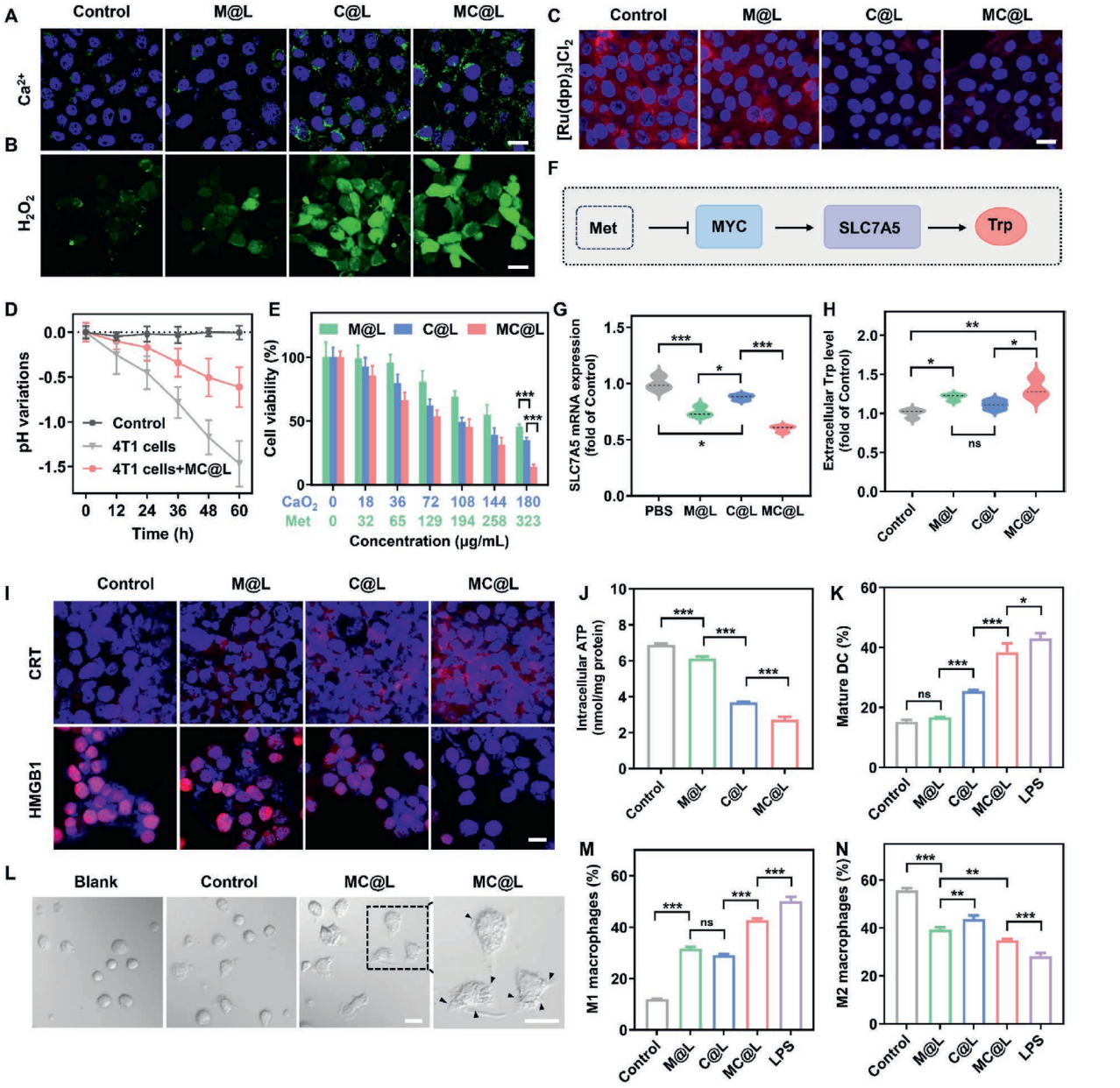

Figure 3 *In vitro* cytotoxicity and immune activation. (A, B) CLSM examination of intracellular Ca^{2+} concentration (A) and H_2O_2 level (B) in 4T1 cells with different treatments. Scale bar = 20 μm. (C) CLSM examination of intracellular O_2 in 4T1 cells under hypoxic conditions with different treatments. Red fluorescence represents the hypoxic level. Scale bar = 20 μm. (D) Extracellular pH variations of 4T1 cells (n = 3). (E) 4T1 cell viability after 48 h incubation with different treatments (n = 5). (F) Schematic diagram illustrating that Met-mediated Trp uptake inhibition. (G) mRNA expressions of *SLC7A5* in 4T1 cells with different treatments analyzed by qPCR (n = 3). (H) ELISA analysis of extracellular Trp levels in the culture medium of 4T1 cells treated with different formulations (n = 3). (I) CLSM examination of CRT exposure and HMGB1 release in 4T1 cells with different treatments. Scale bar = 20 μm. (J) Quantitative analysis of intracellular ATP concentration in 4T1 cells with different treatments (n = 3). (K) Quantitative analysis of *in vitro* DC maturation after incubation with 4T1 cells pretreated with different formulations (n = 3). (L) The optical images of DCs with different treatments. Scale bar = 20 μm. (M, N) Flow cytometry examination of M1 macrophages ($CD11b^+F4/80^+CD86^+$) (M) and M2 macrophages ($CD11b^+F4/80^+CD206^+$) (N) after different treatments. Data are presented as mean ± SD (n = 3). *P < 0.05, **P < 0.01, ***P < 0.001. ns, no significance.

observed in *in vitro* experiments, the tumor vascular normalization effect was further evaluated in the 4T1 tumor-bearing BALB/c model. As shown in Fig. 4A, the eNOS expression levels in tumor tissues were enhanced in M@L and C@L groups compared to the control group. The synergistic treatment of Met and CaO_2 (MC@L group) exhibited remarkably increased eNOS expression level, which provided the potential for achieving vascular normalization *in vivo*. The activation of eNOS led to significant NO generation in tumor vascular ECs, which was beneficial for restoring perivascular NO gradients (Fig. 4B and Supporting Information Fig. S17A and S17B). As reported by the research, selective maintenance of NO gradients around tumor vessels was

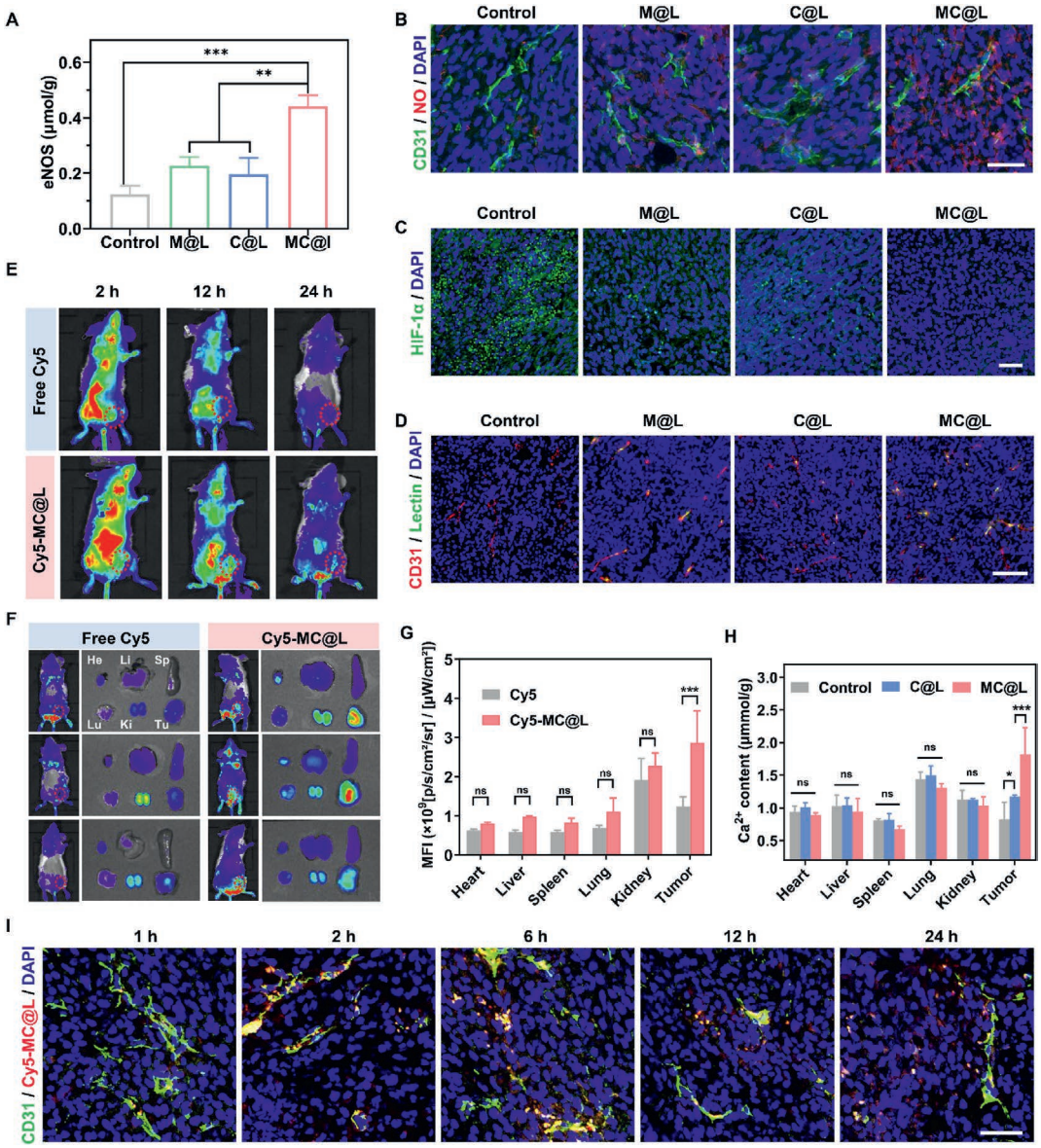

Figure 4 *In vivo* vascular normalization and biodistribution. (A) eNOS protein expression levels in tumor tissues with different treatments. (B) The distribution of NO (red) and tumor vessels (green) in tumor tissues with different treatments. Scale bar = 50 μm. (C) Representative immunofluorescent images of HIF-1α expression (green) in tumor tissues with different treatments. Scale bar = 50 μm. (D) The perfusion of tumor vessels after different treatments. Scale bar = 100 μm. (E) *In vivo* fluorescence images of 4T1 tumor-bearing mice at different time points after intravenous injection of free Cy5 or Cy5-MC@L. (F) *In vivo* fluorescence images of 4T1 tumor-bearing mice at 24 h post-injection and *ex vivo* fluorescence images of major organs and tumor tissues harvested at 24 h post-injection. (G) The corresponding quantification of mean fluorescence intensity (MFI) values of *ex vivo* major organs and tumor tissues ($n = 3$). (H) The content of Ca^{2+} in major organs and tumor tissues of 4T1 tumor-bearing mice at 24 h post-injection of C@L or MC@L. Data are presented as mean ± SD ($n = 3$). (I) The co-localization of Cy5-MC@L (red) and tumor vessels (green) at different times. Scale bar = 50 μm $^*P < 0.05$, $^{**}P < 0.01$, $^{***}P < 0.001$. ns, no significance.

essential for normalizing distorted tumor vasculature[5]. In order to better evaluate the direct anti-angiogenesis effect, the mean vessel density (MVD) was subsequently examined. As shown in Fig. S17C, M@L and C@L groups both exhibited decreased MVD along with reduced expressions of the angiogenic factors VEGF and HIF-1α (Fig. S17D and Fig. 4C), indicating that the restoration of the perivascular NO gradients exerted anti-angiogenesis and vascular maturation effects, thus favoring the alleviation of hypoxia in TME. Aside from studying the structure changes, the function of tumor vessels was also analyzed by intravenously injecting FITC-labelled lycopersicon esculentum lectin to evaluate the tumor perfusion capability. According to Fig. 4D, MC@L group exhibited the highest lectin perfusion, which benefited from the NO generation and vascular maturation.

The ordered tumor vessels with mature structure and elevated perfusion function were closely correlated with higher oxygen and medicine delivery as well as distribution. Thereupon, the *in vivo* biodistribution of Cy5-labelled MC@L (designated as Cy5-MC@L) was subsequently analyzed using In vivo Imaging System (IVIS) at different time points. As shown in Fig. 4E, Cy5-

MC@L exhibited much higher accumulation in the tumor region compared to the free Cy5 group. It was worth noting that the tumor tissue-located fluorescence in Cy5-MC@L group still maintained at a higher level than that in other major organs 24 h post-injection, while the fluorescence of free Cy5 group mainly accumulated in kidney (Fig. 4F and G). In addition, the Ca^{2+} content in tumor tissue of MC@L group was more significant than that of control and C@L groups (Fig. 4H), which was ascribed to the intrinsic ATR effect of NPs and the tumor vascular normalization-mediated perfusion enhancement (Fig. 4D). Besides, no significant Ca^{2+} accumulation was observed in major organs among C@L and MC@L groups, ensuring the biosafety of our lipid nano delivery system (Fig. 4H).

As verified at the cellular level, vascular ECs were available to mediate transcytosis (Fig. 2J and L), which was important for transferring therapeutic agents into the tumor bed for antitumor therapy. In order to explore whether transcytosis also existed in animal models, the colocalization condition of intravenously injected Cy5-MC@L and tumor vessels at different points was further analyzed using the immunostaining method. As indicated in Fig. 4I, the red fluorescence of Cy5-MC@L was majorly colocalized with tumor vessels within 6 h after injection, and the intensity of red fluorescence increased as time went by. After 6 h post-injection, obvious red fluorescence signals were observed in perivascular regions. Consistently, the colocalization constants of Cy5-MC@L and CD31 also decreased with time, indicating Cy5-MC@L was successfully transported out of the blood vessels as time extended (Supporting Information Fig. S18). The successful transcytosis effect in the tumor region ensured subsequent antitumor effects.

3.6. *Antitumor efficacy*

Abnormal tumor vasculature negatively influences the antitumor therapeutic efficacy by hampering drug delivery and constructing the immunosuppressive TME. To evaluate the manner in which tumor vascular normalization triggered by activating eNOS would enhance Ca^{2+} overload-mediated therapeutic modality, we next explored the antitumor efficiency in a unilateral BALB/c tumor model (Fig. 5A). In this section, we supplemented two PD-L1

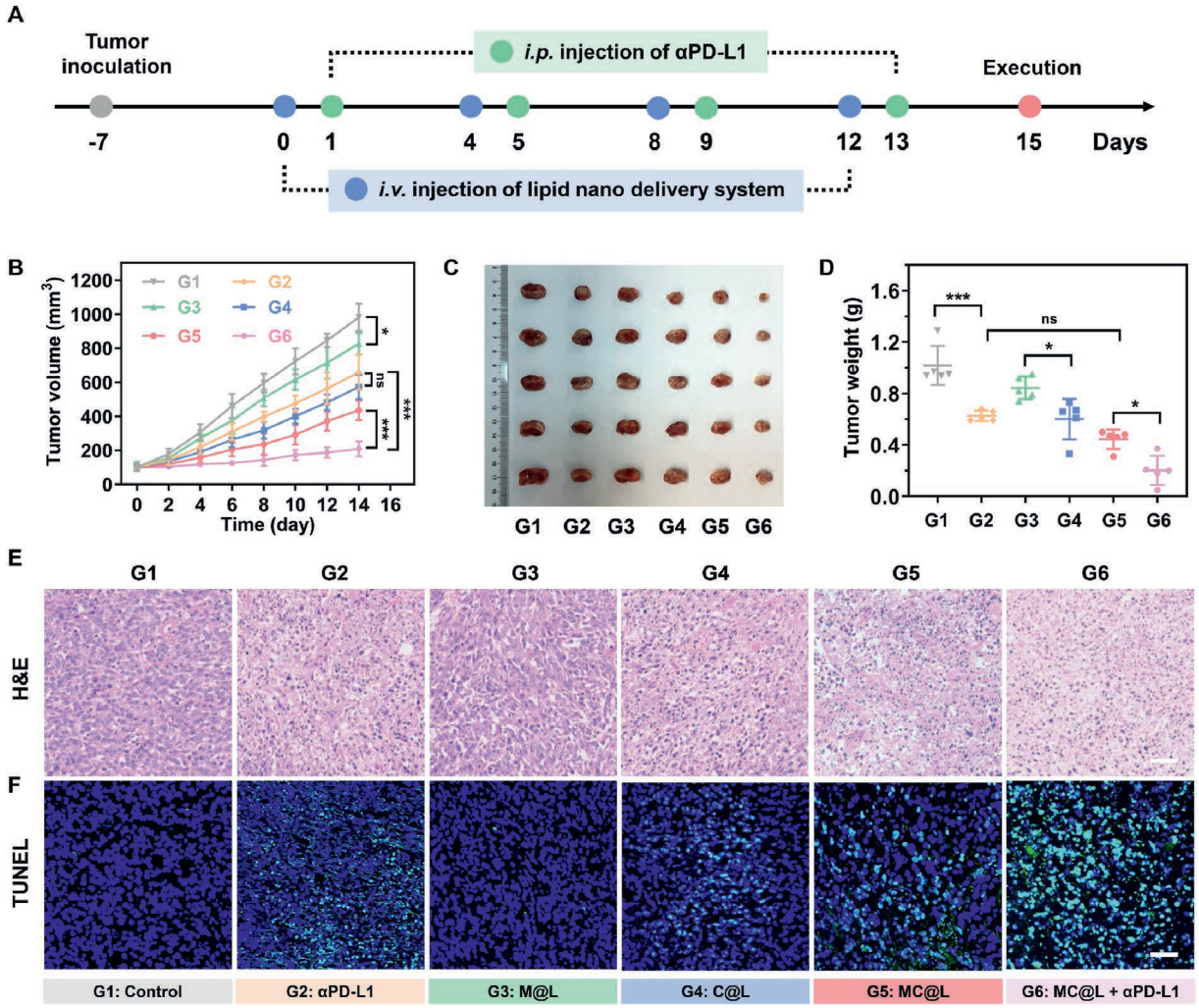

Figure 5 *In vivo* antitumor efficacy. (A) Treatment schedule for *in vivo* antitumor efficacy in the unilateral 4T1 tumor-bearing mice model. i.p., intraperitoneal. i.v., intravenous. (B) Tumor growth curves of the unilateral 4T1 tumor-bearing mice (G1: Control; G2: αPD-L1; G3: M@L; G4: C@L; G5: MC@L; G6: MC@L+αPD-L1) ($n = 5$). (C and D) Photograph (C) and the corresponding weights (D) of the resected tumors in different groups at the end of treatment. Data are presented as mean ± SD ($n = 5$). (E and F) H&E (E) and TUNEL (F) staining images of the tumor tissues in different groups. Scale bar = 50 μm (F). *$P < 0.05$, **$P < 0.01$, ***$P < 0.001$. ns, no significance.

antibody-containing groups (αPD-L1 group and MC@L+αPD-L1 group) to better assess the improvement of immunosuppressive TME. As shown in Fig. 5B−D and Supporting Information Fig. S19, single treatment with the PD-L1 antibody was hard to suppress tumor growth, which was mainly ascribed to the low infiltration and activation of immune cells. However, after combining MC@L with PD-L1 antibody treatment, the tumor volumes could be successfully restricted to a small size. Such an excellent tumor inhibitory effect was beneficial from the advantages of Met and CaO_2-mediated tumor vascular normalization to a great extent. The different levels of tumor cell apoptosis and necrosis in hematoxylin and eosin (H&E) staining, and terminal deoxynucleotidyl transferase dUTP nick-end labeling (TUNEL) staining results further demonstrated the synergistic effect of Met and CaO_2, and the elevated antitumor therapeutic efficiency enhanced by MC@L compared to single treatment of αPD-L1 (Fig. 5E and F). All the groups with different treatments exhibited no obvious body weight changes (Supporting Information Fig. S20) or damage in major organs (Supporting Information Fig. S21), indicating the good biosafety of the lipid nano delivery system.

3.7. *In vivo immune activation*

Given the identification that Ca^{2+} overload and oxidative stress caused by CaO_2 in tumor cells could arouse ICD by accelerating the release of DAMPs[31,35], which further function as potent activators to boost tumor cell immunogenicity, the *in vivo* ICD induction effect was subsequently verified. As indicated in Fig. 6A,

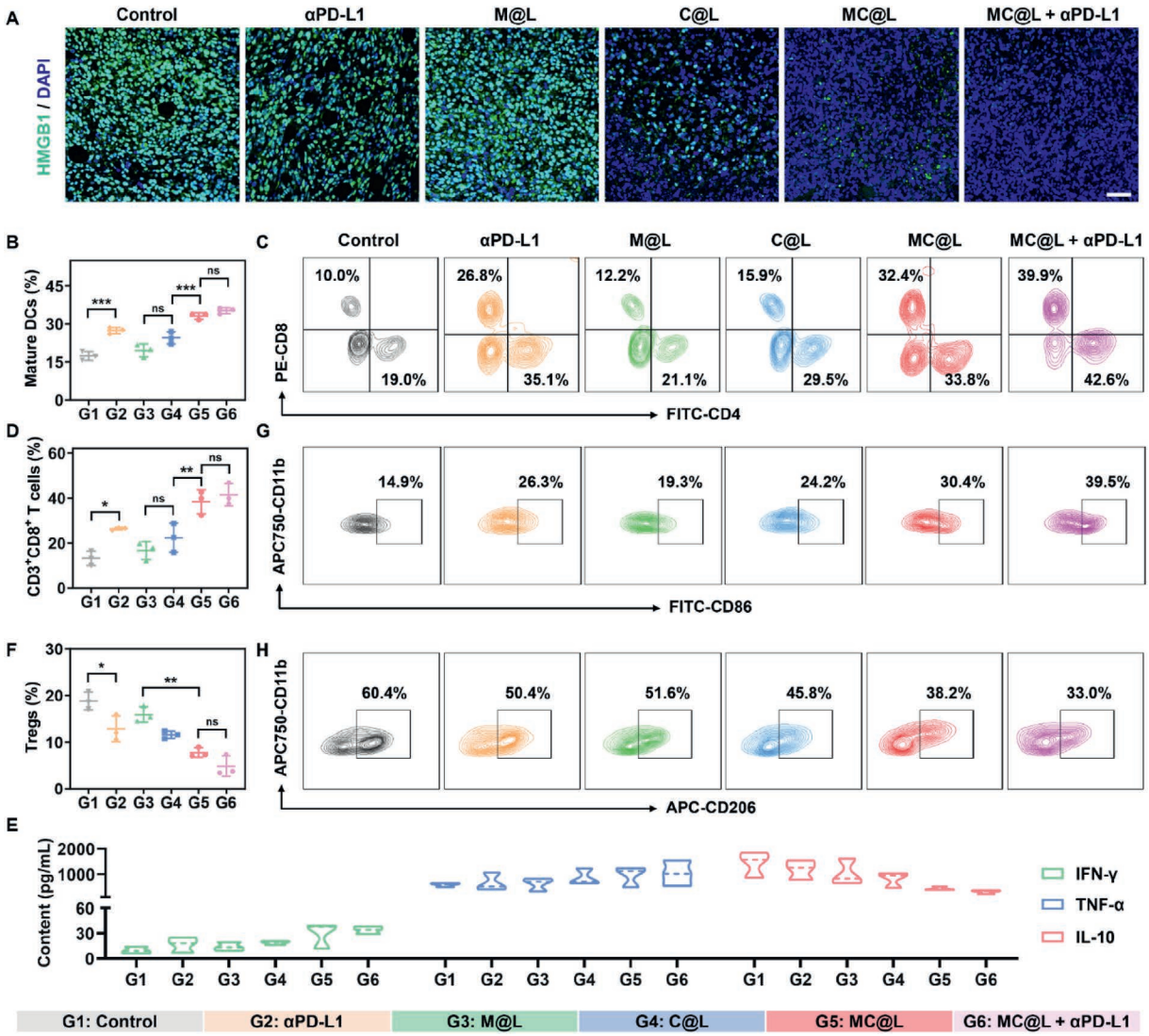

Figure 6 *In vivo* immune activation. (A) Representative immunofluorescent images of HMGB1 release in tumor tissues with different treatments. Scale bar = 50 μm. (B) Quantification of mature DCs in the TDLNs of 4T1 tumor-bearing mice post-treatments (G1: Control; G2: αPD-L1; G3: M@L; G4: C@L; G5: MC@L; G6: MC@L+αPD-L1) (n = 3). (C) Flow cytometry examination of intratumorally infiltrated $CD4^+$ T cells ($CD4^+$, gated on $CD3^+$) and $CD8^+$ T cells ($CD8^+$, gated on $CD3^+$) post-treatments. (D) Quantification of intratumorally infiltrated $CD8^+$ T cells of 4T1 tumor-bearing mice post-treatments (n = 3). (E) The heatmaps of the content of IFN-γ, TNF-α, and IL-10 within the tumor tissues post-treatments (n = 3). (F) Quantification of intratumorally infiltrated Treg cells of 4T1 tumor-bearing mice post-treatments. Data are presented as mean ± SD (n = 3). (G, H) Flow cytometry examination of intratumorally infiltrated M1 macrophages ($CD11b^+CD86^+$, gated on $CD11b^+F4/80^+$) (G) and M2 macrophages ($CD11b^+CD206^+$, gated on $CD11b^+F4/80^+$) (H) post-treatments. *P < 0.05, **P < 0.01, ***P < 0.001. ns, no significance.

the CaO_2-contained groups could significantly promote HMGB1 release from tumor cell nuclei, thus serving as "danger" signals to promote the recruitment and activation of immune effector cells. Benefiting from DMAPs-mediated enhancement of tumor cell immunogenicity and "normalized" tumor vascular remodeling to relieve hypoxic environment with lower acidity but higher immune cells infiltration, the maturation rates of DCs in tumor-draining lymph nodes (TDLNs) of MC@L significantly increased compared to control group (Fig. 6B and Supporting Information Fig. S22), and the DC maturation rate of MC@L+αPD-L1 reached 35.27 $\pm$ 1.14%, much better than that of single αPD-L1 treatment (27.43 $\pm$ 1.22%).

Moreover, the intratumoral infiltrated $CD4^+$ helper T cells and $CD8^+$ cytotoxic T cells, which performed antitumor roles by secreting cytokines or mediating direct tumor cell killing effect, were also analyzed (Fig. 6C and D, and Supporting Information Fig. S23 and S24). In comparison to the control group, M@L and C@L exhibited much higher percentages of $CD4^+$ helper T cells and $CD8^+$ cytotoxic T cells. Such phenomena could be respectively ascribed to Met-mediated tumor cells' Trp engulfment inhibition that further led to the decrease of Kyn, a downstream immunosuppressive metabolite that hampers the activity of T cells, and CaO_2-induced ICD, which further benefited immune cells recruitment and activation by releasing a large number of tumor antigens and DAMPs. It was worth noting that single αPD-L1 treatment exhibited higher percentages of $CD4^+$ helper T cells and $CD8^+$ cytotoxic T cells than M@L and C@L groups, consistent with the result of mature DCs, which are responsible for presenting processed tumor antigens to T cells. Nevertheless, the levels of intratumoral infiltrated $CD4^+$ helper T cells and $CD8^+$ cytotoxic T cells were significantly increased under the cascaded combination of Met and CaO_2 (MC@L) than single αPD-L1 treatment, accompanied by remarkably upregulated pro-inflammatory cytokines including tumor necrosis factor-α (TNF-α) and interferon-γ (IFN-γ) (Fig. 6E), illustrating the synergetic effect of Met and CaO_2 in reversing immunosuppressive TME. The lower percentages of Treg populations and cytokine interleukin-10 (IL-10) content in MC@L than αPD-L1 group (Fig. 6E and F, and Supporting Information Fig. S25) could additionally demonstrate the excellent antitumor immunity by the synergetic effect of Met and CaO_2.

As another type of important tumor-infiltrated immune cells that engage in tumor progression, TAMs that possessed two major phenotypes, including anti-tumor M1 phenotype and pro-tumor M2 phenotype, were analyzed as well. According to the past studies[1,34] and our verification at the cellular level (Fig. 3M and N), hypoxia alleviation was conducive to reprogramming M2 macrophages toward M1 phenotype, thus promoting antitumor efficacy. Under *in vivo* environment, both O_2 generated by CaO_2 degradation and blood O_2 transport promoted by eNOS-activated tumor vascular normalization contributed to hypoxia alleviation, thus C@L group exhibited much higher M1 percentage and less M2 percentage than M@L group (Fig. 6G and H, and Supporting Information Figs. S26 and S27), which was different from that at cellular level, whose reprogramming effect was mainly counted on CaO_2-mediated O_2 generation and Met-mediated AMPK−NF-κB signaling pathway. It was noteworthy that compared to single αPD-L1 therapy, MC@L treatment could significantly enhance the M2 repolarization efficiency of αPD-L1, proving the excellent synergistic effect of CaO_2 and Met in reversing the immunosuppressive TME.

4. Conclusions

Selectively localizing NO around blood vessels and restoring perivascular NO gradients could normalize tumor vasculature to improve O_2 and drug delivery and immune cells infiltration. Instead of exogenously delivering NO donors, which are challenged with a steady NO release profile and NO aggregation at the far tumor regions rather than vascular ECs, we designed a lipid nano delivery system, MC@L, and utilized endothelial transcytosis to deliver CaO_2 and Met into tumor vascular ECs and tumor cells, enabling tumor vascular normalization by increasing the activity of eNOS *via* Ca^{2+}-promoted eNOS coupling, as well as Ca^{2+} and Met-mediated AMPK−eNOS signaling pathway. In addition, MC@L undergoing transcytosis could further be internalized by tumor cells to degrade into Ca^{2+} and Met in the acidic lysosomes. CaO_2-induced ICD and Met-mediated inhibition of Trp uptake in tumor cells supported the reversion of immunosuppressive TME, which was available to arouse stronger antitumor immune responses with the aid of O_2 generation and H^+ consumption during CaO_2 degradation, thus greatly enhancing PD-L1 blockade efficacy. In summary, by precisely localizing NO around tumor vessels *via* activating eNOS of tumor vascular ECs, together with ICD induction, this lipid nano delivery system could effectively enhance the tumor immunogenicity for robust antitumor immunity.

Acknowledgments

The authors gratefully acknowledge the support of this research by National Natural Science Foundation of China (32171313, 32322043), Shenzhen Science and Technology Program (RCYX20210706092104033, China).

Author contributions

Huisong Hao: Methodology, Validation, Investigation, Data curation, Formal analysis, Writing-original draft. Yunfei Yi: Conceptualization, Methodology, Investigation, Validation, Data curation, Writing-original draft. Yanan Fu: Methodology, Investigation, Validation. Shengjie Sun: Methodology, Investigation, Validation. Zhangwen Peng: Methodology, Investigation, Validation. Jia Tang: Investigation, Validation, Supervision. Yixuan Fang: Investigation, Validation, Supervision. Shihao Zhuang: Investigation, Validation, Supervision. Yaqi Ouyang: Investigation, Validation, Supervision. Tianqi Wang: Conceptualization, Resources, Supervision, Writing-review & editing. Meiying Wu: Resources, Supervision, Funding acquisition, Project administration, Writing-review & editing.

Conflicts of interest

The authors have no conflicts of interest to declare.

Appendix A. Supporting information

Supporting information to this article can be found online at https://doi.org/10.1016/j.apsb.2025.11.040.

References

1. Yi YF, Yu M, Feng C, Hao HS, Zeng WW, Lin CC, et al. Transforming "cold" tumors into "hot" ones *via* tumor-microenvironment-responsive

siRNA micelleplexes for enhanced immunotherapy. *Matter* 2022;**5**: 2285−305.
2. Jain RK. Normalizing tumor vasculature with anti-angiogenic therapy: a new paradigm for combination therapy. *Nat Med* 2001;**7**:987−9.
3. Martin JD, Cabral H, Stylianopoulos T, Jain RK. Improving cancer immunotherapy using nanomedicines: progress, opportunities and challenges. *Nat Rev Clin Oncol* 2020;**17**:251−66.
4. Sung YC, Jin PR, Chu LA, Hsu FF, Wang MR, Chang CC, et al. Delivery of nitric oxide with a nanocarrier promotes tumour vessel normalization and potentiates anti-cancer therapies. *Nat Nanotechnol* 2019;**14**:1160−9.
5. Wu JB, Tang YL, Liang XH. Targeting VEGF pathway to normalize the vasculature: an emerging insight in cancer therapy. *OncoTargets Ther* 2018;**11**:6901−9.
6. Kashiwagi S, Tsukada K, Xu L, Miyazaki J, Kozin SV, Tyrrell JA, et al. Perivascular nitric oxide gradients normalize tumor vasculature. *Nat Med* 2008;**14**:255−7.
7. Calvert JW, Gundewar S, Jha S, Greer JJ, Bestermann WH, Tian R, et al. Acute metformin therapy confers cardioprotection against myocardial infarction *via* AMPK−eNOS-mediated signaling. *Diabetes* 2008;**57**:696−705.
8. Fleming I, Busse R. Signal transduction of eNOS activation. *Cardiovasc Res* 1999;**43**:532−41.
9. Gielis JF, Lin JY, Wingler K, Van Schil PEY, Schmidt HH, Moens AL. Pathogenetic role of eNOS uncoupling in cardiopulmonary disorders. *Free Radic Biol Med* 2011;**50**:765−76.
10. Tran N, Garcia T, Aniqa M, Ali S, Ally A, Nauli SM. Endothelial nitric oxide synthase (eNOS) and the cardiovascular system: in physiology and in disease states. *Am J Biomed Sci Res* 2022;**15**: 153−77.
11. Sessa WC. eNOS at a glance. *J Cell Sci* 2004;**117**:2427−9.
12. Kim J, Yang G, Kim YJ, Kim J, Ha J. AMPK activators: mechanisms of action and physiological activities. *Exp Mol Med* 2016;**48**:e224.
13. Rodríguez C, Muñoz M, Contreras C, Prieto D. AMPK, metabolism, and vascular function. *FEBS J* 2021;**288**:3746−71.
14. Bertrand N, Wu J, Xu XY, Kamaly N, Farokhzad OC. Cancer nanotechnology: the impact of passive and active targeting in the era of modern cancer biology. *Adv Drug Deliv Rev* 2014;**66**:2−25.
15. Zhu MS, Zhuang J, Li Z, Liu QQ, Zhao RP, Gao ZX, et al. Machine-learning-assisted single-vessel analysis of nanoparticle permeability in tumour vasculatures. *Nat Nanotechnol* 2023;**18**:657−66.
16. Dasgupta A, Sofias AM, Kiessling F, Lammers T. Nanoparticle delivery to tumours: from EPR and ATR mechanisms to clinical impact. *Nat Rev Bioeng* 2024;**2**:714−6.
17. Zhou Q, Li JJ, Xiang JJ, Shao SQ, Zhou ZX, Tang JB, et al. Transcytosis-enabled active extravasation of tumor nanomedicine. *Adv Drug Deliv Rev* 2022;**189**:114480.
18. Yu M, Zeng WW, Ou Yang YQ, Liang S, Yi YF, Hao HS, et al. ATP-exhausted nanocomplexes for intratumoral metabolic intervention and photoimmunotherapy. *Biomaterials* 2022;**284**:121503.
19. Huang XW, Sun TT, Wang JL, Hong XL, Chen HM, Yan TT, et al. Metformin reprograms tryptophan metabolism to stimulate $CD8^+$ T-cell function in colorectal cancer. *Cancer Res* 2023;**83**:2358−71.
20. Shen S, Mamat M, Zhang S, Cao J, Hood ZD, Figueroa Cosme L, et al. Synthesis of CaO_2 nanocrystals and their spherical aggregates with uniform sizes for use as a biodegradable bacteriostatic agent. *Small* 2019;**15**:1902118.
21. Wang HF, Zhao YS, Li TY, Chen Z, Wang YN, Qin CY. Properties of calcium peroxide for release of hydrogen peroxide and oxygen: a kinetics study. *Chem Eng J* 2016;**303**:450−7.
22. Zhang M, Song RX, Liu YY, Yi ZG, Meng XF, Zhang JW, et al. Calcium-overload-mediated tumor therapy by calcium peroxide nanoparticles. *Chemistry* 2019;**5**:2171−82.
23. Hao HS, Yu M, Yi YF, Sun SJ, Huang XY, Huang CY, et al. Mesoporous calcium peroxide-ignited NO generation for amplifying photothermal immunotherapy of breast cancer. *Chem Eng J* 2022;**437**: 135371.
24. Lin CC, Huang CY, Shi ZQ, Ou MT, Sun SJ, Yu M, et al. Biodegradable calcium sulfide-based nanomodulators for H_2S-boosted Ca^{2+}-involved synergistic cascade cancer therapy. *Acta Pharm Sin B* 2022;**12**:4472−85.
25. Xue Yang Meng, Cong Cong, Bian Jia Xin, Xu Zi Chuang, Liu Xiao Kang, Liu Lan Xiang, et al. Nanodrugs detonate lysosome bombs. *Front Pharmacol* 2022;**13**:909504.
26. Borkowska M, Siek M, Kolygina DV, Sobolev YI, Lach S, Kumar S, et al. Targeted crystallization of mixed-charge nanoparticles in lysosomes induces selective death of cancer cells. *Nat Nanotechnol* 2020; **15**:331−41.
27. Song Y, Zhang HX, Wang X, Geng X, Sun YQ, Liu J, et al. One stone, three birds: pH triggered transformation of aminopyronine and iminopyronine based lysosome targeting viscosity probe for cancer visualization. *Anal Chem* 2021;**93**:1786−91.
28. Oberley TD, Oberley LW. Antioxidant enzyme levels in cancer. *Histol Histopathol* 1997;**12**:525−35.
29. Nakamura H, Takada K. Reactive oxygen species in cancer: current findings and future directions. *Cancer Sci* 2021;**112**:3945−52.
30. Platten M, Nollen EAA, Röhrig UF, Fallarino F, Opitz CA. Tryptophan metabolism as a common therapeutic target in cancer, neurodegeneration and beyond. *Nat Rev Drug Discov* 2019;**18**:379−401.
31. Huang C, Lin BQ, Chen CY, Wang HM, Lin XS, Liu JM, et al. Synergistic reinforcing of immunogenic cell death and transforming tumor-associated macrophages *via* a multifunctional cascade bioreactor for optimizing cancer immunotherapy. *Adv Mater* 2022;**34**: 2207593.
32. Pu KY, Zhang Y. Transformable nanosensitizer with tumour microenvironment-activated sonodynamic process and calcium release for enhanced cancer immunotherapy. *Angew Chem Int Ed Engl* 2021; **60**:14051−9.
33. Sun SJ, Yu M, Yu L, Huang WX, Zhu MS, Fu YN, et al. Nrf2 silencing amplifies DNA photooxidative damage to activate the STING pathway for synergistic tumor immunotherapy. *Biomaterials* 2023;**296**:122068.
34. Zeng WW, Yu M, Chen T, Liu YQ, Yi YF, Huang CY, et al. Polypyrrole nanoenzymes as tumor microenvironment modulators to reprogram macrophage and potentiate immunotherapy. *Adv Sci (Weinh)* 2022;**9**:e2201703.
35. Wang MX, Xue FF, An L, Wu D, Sha S, Huang G, et al. Photoacoustic-imaging-guided photothermal regulation of calcium influx for enhanced immunogenic cell death. *Adv Funct Mater* 2024;**34**: 2311853.